What is the Mechanism for the Modification of Convective Cloud Distributions by Land Surface–Induced Flows?

Luis Garcia-Carreras and Douglas J. Parker

Institute for Climate and Atmospheric Science, University of Leeds, Leeds, United Kingdom

John H. Marsham

National Centre for Atmospheric Science, University of Leeds, Leeds, United Kingdom

ABSTRACT

The aim of this study is to determine the mechanism that modulates the initiation of convection within convergence zones caused by land surface–induced mesoscale flows. An idealized modeling approach linked quantitatively to observations of vegetation breezes over tropical Benin was used. A large-eddy model was used with a prescribed land surface describing heterogeneities between crop and forest over which vegetation breezes have been observed. The total surface fluxes were constant but the Bowen ratio varied with vegetation type. The heterogeneous land surface created temperature differences consistent with observations, which in turn forced mesoscale winds and convection at the convergence zones over the crop boundaries. At these convergence zones optimum conditions for the initiation of convection were found in the afternoon; the equivalent potential temperature was higher in the convergence zones than over anywhere else in the domain, due to reduced entrainment, and the mesoscale convergence produced a persistent increase in vertical wind velocities of up to 0.5 m s^{-1} over a 5–10-km region. The relative importance of these two mechanisms depended on the synoptic conditions. When convective inhibition was weak, the thermodynamic conditions at the convergence zone were most important, as the triggering of convection was easily accomplished. However, when the thermodynamic profile inhibited convection, the mesoscale updrafts became essential for triggering in order to break through the inhibiting barrier. At the same time, subsidence over the forest produced a warm capping layer over the boundary layer top that suppressed convection over the forest throughout the afternoon.

1. Introduction

Mesoscale variations in land surface type affect the surface energy budget, via changes in Bowen ratio and albedo, in turn leading to variations in low-level temperatures (Pielke 2001; Betts et al. 2007). One of the impacts of the temperature gradients that are formed at land surface type boundaries is the initiation of mesoscale flows analogous to sea breezes (Segal and Arritt 1992).

A wide range of modeling studies have looked at the impact of land surface–induced flows (e.g., Ookouchi et al. 1984; Segal et al. 1988; Avissar and Schmidt 1998; Weaver and Avissar 2001; Roy and Avissar 2002; Weaver 2004b). Earlier studies suggested that synoptic conditions

needed to be weak for such flows to develop (Avissar and Schmidt 1998). More recently, however, various studies with more sophisticated land surface schemes and realistic synoptic conditions suggest that stronger synoptic winds will alter the shape and orientation of such flows, but not necessarily their strength (Weaver 2004b; Roy and Avissar 2002). In the case of Roy and Avissar (2002) and Weaver and Avissar (2001), the model results were also validated by satellite cloud observations. Large-eddy simulations have shown similar results, although in these cases the role of the orientation of the background flow with respect to the surface heterogeneities, as well as its strength, was highlighted (Raasch and Harbusch 2001; Kim et al. 2004; Prabha et al. 2007).

One of the most important impacts of such land surface–induced flows is on the initiation of convection, as this can lead to potential feedbacks onto the surface via radiative effects or the alteration of rainfall patterns. Some modeling studies have found that when synoptic

Corresponding author address: Luis Garcia-Carreras, School of Earth and Environment, University of Leeds, Leeds LS29JT, United Kingdom.
E-mail: eelgc@leeds.ac.uk

conditions were favorable, winds forced by surface heterogeneity in soil moisture (Chen and Avissar 1994; Trier et al. 2004; Weaver 2004a; Frye and Mote 2010), cloud shading (Marsham et al. 2007a,b), and vegetation (Wang et al. 2000; Roy and Avissar 2002; Kawase et al. 2008; Roy 2009) led to enhanced shallow, and sometimes even deep, convection at the convergence zones. These studies highlighted that the vertical motions at the convergence zones, as well as the vertical fluxes of heat and moisture, were significant, and sometimes larger than the turbulent fluxes.

Other studies, however, disagree with the idea that mesoscale flows can induce significant vertical speeds or fluxes when compared to their turbulent counterparts—for example, when comparing domain-average profiles for homogeneous and heterogeneous land surfaces (Zhong and Doran 1998; Doran and Zhong 2000; Kang and Davis 2008). In the case of Zhong and Doran (1998) and Doran and Zhong (2000), this can be attributed to the relatively coarse resolution used compared to other studies (Weaver 2009; Kang and Davis 2009). Another reason for the observed discrepancies could be due to the fact that domain-average fluxes do not take into account any spatial variability that may arise from the mesoscale component or the asymmetry between narrow updrafts and broader subsidence. For example, Patton et al. (2005) found in a large-eddy simulation coupled to a land surface model that although the total mixing ratio vertical fluxes remain unchanged between a heterogeneous and homogeneous land surface, the relative contribution from mesoscale and turbulent components did vary, presumably as a result of a change in their spatial distribution. Aircraft observations have also shown that although vertical transport from inland breezes is not large, it is significant at the leading edge of the front (Mahrt et al. 1994). Mesoscale boundary layer convergence from other sources has been associated with the initiation of clouds and storms (Wilson and Schreiber 1986; Ziegler and Rasmussen 1998) as storm development is very sensitive to the updraft strength (Fabry 2006). It is therefore likely that even strictly local effects caused by land surface–induced convergence can then extend over a larger area via their impact on convection.

Observational evidence of land surface–induced flows, although relatively scarce, has slowly been growing. A variety of studies, for example, have inferred the presence of vegetation-induced flows via the presence of persistent mean cross-boundary winds between crops and native vegetation (Smith et al. 1994; Doran et al. 1995; Souza et al. 2000). More significantly, aircraft observations of such features forced by soil moisture (Taylor et al. 2007; Kang et al. 2007), albedo anomalies (Marsham et al. 2008), cloud shading (Marsham et al. 2007a,b), and vegetation

patterns (Garcia-Carreras et al. 2010) now exist. For example, in Garcia-Carreras et al. (2010) a wind pattern persistent over 2 h is observed associated with boundaries between protected forest and agricultural land in West Africa. These winds are associated with land surface patches larger than 4 km and lead to enhanced convection over the cropland regions. Taylor et al. (2010) also document a case of a mesoscale convective system triggered on a soil-moisture gradient in the Sahel, thus showing how mesoscale features can affect the larger scales. The link between land cover and convection has been extensively corroborated by a variety of satellite climatologies linking low-level cloud cover and deforested regions (Cutrim et al. 1995; Wang et al. 2000; Roy and Avissar 2002; Wang et al. 2009; Garcia-Carreras et al. 2010) or areas of crop (Brown and Arnold 1998; Rabin et al. 1990), consistent with initiation of convection caused by land surface–induced flows.

The potential impact of vegetation breezes on cloudiness, and thus rainfall, is critical for a proper understanding of the long-term impacts of deforestation. While many general circulation models (GCMs) find that deforestation leads to a significant decrease in rainfall (McGuffie et al. 1995; Zhang et al. 2001; Werth and Avissar 2002, among others), the assumed conversion from forest to pasture is often unrealistic (Pielke et al. 2007) and, perhaps crucially, mesoscale phenomena remain unresolved. Remote sensing observations of rainfall as well as rain gauge data in Amazonia suggest a consistent increase in rainfall despite the ongoing deforestation, particularly over the deforested regions (Chu et al. 1994; Chen et al. 2001; Negri et al. 2004). One potential reason for the discrepancy is the mesoscale impact, as vegetation breezes could act as a negative feedback promoting plant growth over the deforested regions during the dry season (Roy 2009).

The link between land surface–induced breezes and cloud cover seems to be robust, particularly from the available satellite and aircraft observations. In these studies the source of initiation of convection associated with land surface–induced flows is usually simply attributed to convergence, but not enough consideration has been given to what exact mechanisms lead to enhanced convection within the convergence zones, particularly given the discrepancies in the literature as to whether the vertical velocities caused by mesoscale convergence zones are significant. To better understand the impact of land surface–induced flows on cloud cover and rainfall, particularly in the presence of different dynamic and thermodynamic synoptic conditions, the cause of the land surface–induced organization of cloud initiation must be better understood. This will be particularly important for understanding the larger-scale impact of such flows, as well as for any attempts to parameterize them in GCMs

unable to resolve such phenomena. This modeling study attempts to address this issue with the use of a large-eddy model, using the aircraft path in Garcia-Carreras et al. (2010) as a test case.

We propose three general mechanisms that could explain how mesoscale convergence promotes convective initiation:

- A purely dynamic response due to increased vertical velocities from the mesoscale convergence, which may enhance thermals in some areas while suppressing them in others.
- A thermodynamic response due to moisture convergence from a cool, moist region (lower Bowen ratio) to a warmer, drier region (higher Bowen ratio). This may provide greater buoyancy to rising parcels.
- Mesoscale convergence may be of secondary importance, and the observed organization could simply be attributed to higher turbulence over warmer regions leading to a higher frequency of cloud-forming thermals.

In section 2 we describe the modeling setup used, followed by a description of the impact of the surface heterogeneity throughout the domain in section 3. In section 4 a single land surface boundary is analyzed in more detail to investigate the cause of the initiation in convection, looking specifically at thermodynamic and dynamic features. The results are then summarized and discussed in section 5.

2. Large-eddy model setup

Version 2.4 of the Met Office Large Eddy Model (LEM; Gray et al. 2001), a high-resolution cloud-resolving model, was used in 2D for the simulations. The LEM is a nonhydrostatic model, with a Boussinesq equation set. The incompressible Boussinesq approximation was used in this study, which uses a reference density that is constant with height. Water vapor and clouds were explicitly modeled, but with no rainfall or radiation. The exclusion of these factors allows the direct impact of the surface flux heterogeneity to be isolated, without the superposition of cold pools, for example, complicating the analysis of the results. A domain of 312.5-km horizontal and 9-km vertical extent was used, with a horizontal resolution of 250 m and a varying vertical resolution (14–240 m over 90 levels). A layer damping the prognostic variables to their horizontal means was applied above 8500 m to reduce the reflection of gravity waves from the upper boundary. The time step is updated by the model every 10 time steps in order to maintain numerical stability, but it varied mostly between 0.1 and 1 s throughout the simulation.

The test case modeled was chosen to coincide with the observations from 17 August 2006 of Garcia-Carreras et al. (2010) in which direct aircraft observations of vegetation-induced flows are described. The 2D model is therefore set up to follow the aircraft track from which the observations were taken. The model was run for 24 h, initialized using vertical profiles of wind velocities, potential temperature, and specific humidity from the European Centre for Medium-Range Weather Forecasts (ECMWF) reanalysis data at 10.125°N, 2.25°E from 0000 UTC 17 August 2006. A random perturbation between ± 0.1 K and ± 0.025 g kg^{-1} was added to each point in order to add a degree of randomness associated with the real atmosphere, as well as to provide sufficient variability to allow the development of turbulence. The 6-hourly ECMWF wind profiles for 17 August were interpolated to give 3-hourly profiles, and the mean winds in the model were relaxed (over a 2 h time scale) to these values to mimic the synoptic conditions observed on that day.

The surface heat fluxes in the model are imposed, and therefore noninteracting, as is common in this kind of model. In reality there will be some impact of the mesoscale winds on the fluxes, which models show to be significant for heterogeneities larger than 18 times the PBL height (Patton et al. 2005), as well as some effect from cloud shading. The model setup used here, however, is capable of reproducing cloud patterns and mesoscale winds consistent with observations, as shown in section 3. Given the focus of this study is on the initiation of convection, and not small-scale features of the circulation, prescribed surface fluxes are expected to be sufficient.

The diurnal cycle of sensible and latent heat fluxes was estimated by taking the average during July and August 2006 of half-hourly surface station data in Nangatchori, Benin (9.65°N, 1.74°E). The mean fluxes will be lower than a clear-day example because of the impact of clouds. The standard deviation of the mean profile was approximately half of the total flux and was assumed to be caused primarily by clouds. We thus increased the mean fluxes by 50% to filter out the cloud impact and approximate a mean clear-day profile. The inset in Fig. 1 shows the diurnal cycle of sensible and latent heat fluxes derived by this method.

The ECMWF data from 17 August were used as described above, together with the average diurnal cycle of surface fluxes applied homogeneously along the domain. This was used as a control run (CTL). The next run (HET) used the same background conditions as CTL, but with horizontally varying surface fluxes approximating the surface cover observed in Garcia-Carreras et al. (2010). The total surface fluxes were kept constant throughout the domain, but the Bowen ratio was varied to correspond to the land surface type. The percentage
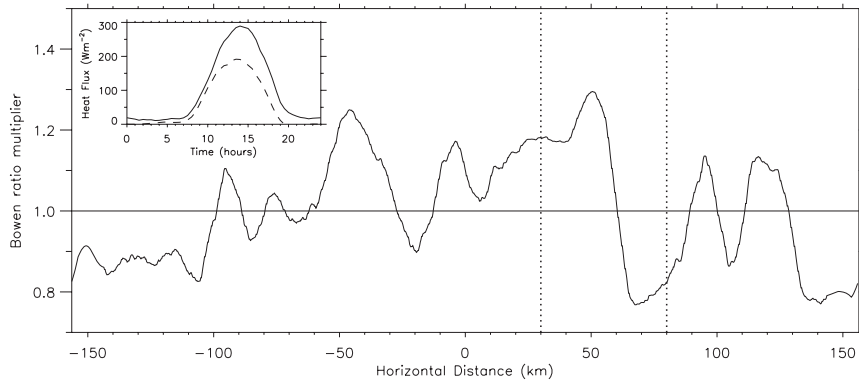
FIG. 1. Bowen ratio multiplier from the homogeneous conditions in HET. The vertical dotted lines show the domain on which section 4 concentrates. The inset shows the sensible (dashed) and latent (solid) heat fluxes imposed in CTL.

of forest/shrub cover along the domain was estimated by using the Globcover land surface product, as in Garcia-Carreras et al. (2010). These values were normalized so that the mean was equal to 1, and the Bowen ratio at each point was adjusted by this value, while keeping the total fluxes constant (Fig. 1). This means that vegetated regions had higher latent heat fluxes, as a result of higher evapotranspiration from the surface, and proportionately lower sensible heat fluxes, which assumes that the surface albedo is constant. The imposed variations in sensible heat fluxes lead to a maximum change of 60 W m^{-2} located between 50 and 65 km in Fig. 1. This variation is consistent or smaller than with other studies, such as 60 W m^{-2} across a vegetation density gradient in Kansas during the First International Satellite Land Surface Climatology Project (ISLSCP) Field Experiment (FIFE; Smith et al. 1994) or up to 150 W m^{-2} in the Amazon (Roy and Avissar 2002). The magnitude of the potential temperature gradients induced by the heterogeneities was also consistent with aircraft observations (see section 3).

The conditions used to initialize the model for these runs was generally favorable for shallow convection, with little, if any, convective inhibition (CIN). The solid red and blue lines in Fig. 2 show the domain-mean temperature and dewpoint temperature profiles in HET at 1200 UTC, illustrating the presence of a low CIN environment and thus widespread shallow cloud presence. The domain-mean values of CIN and convective available potential energy (CAPE) in HET at 1200 UTC were 0.04 and 468 J kg^{-1} computed for a source parcel at 50 m. Another two runs (HICIN and HICINCTL, with a heterogeneous and homogenous surface respectively) were also performed to look at whether the role of the vegetation-induced mesoscale flows was different when conditions were less favorable to convection. To do this, the initial potential temperature profile was increased by

3 K in order to create a more stable profile and thus higher CIN in the domain. The domain-mean values of CIN and CAPE in HICIN at 1200 UTC were 32 and 76 J kg^{-1}, respectively. Figure 2 (dashed lines) shows how this leads to a more stable profile, with some CIN present, and thus inhibition of convective activity, so that clouds appear only from approximately 1600 UTC, when the PBL has developed sufficiently.

The use of a 2D model in this study will have the biggest impact for processes where the surface of interaction matters, for example for entrainment into cumulus clouds. Because of this, the development of convection, particularly into deep convection, may not be well represented (Petch et al. 2008). On the other hand, domain-mean values of cloud cover, as well as the vertical velocity variance in the lower troposphere, have been shown to be less sensitive to the extra dimension (Khairoutdinov and Randall 2003; Xu et al. 2002). When using 2D surface heterogeneities the use of a 2D model
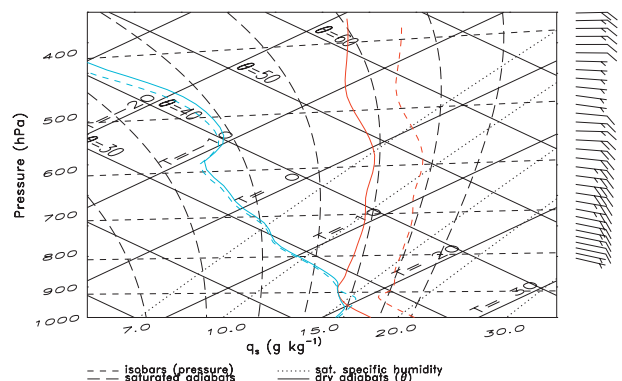

FIG. 2. Tephigram showing the domain-mean temperature (red) and dewpoint temperature (blue) profiles at 1200 UTC in HET (solid) and HICIN (dashed). The wind barbs show the domain-mean winds in HET.
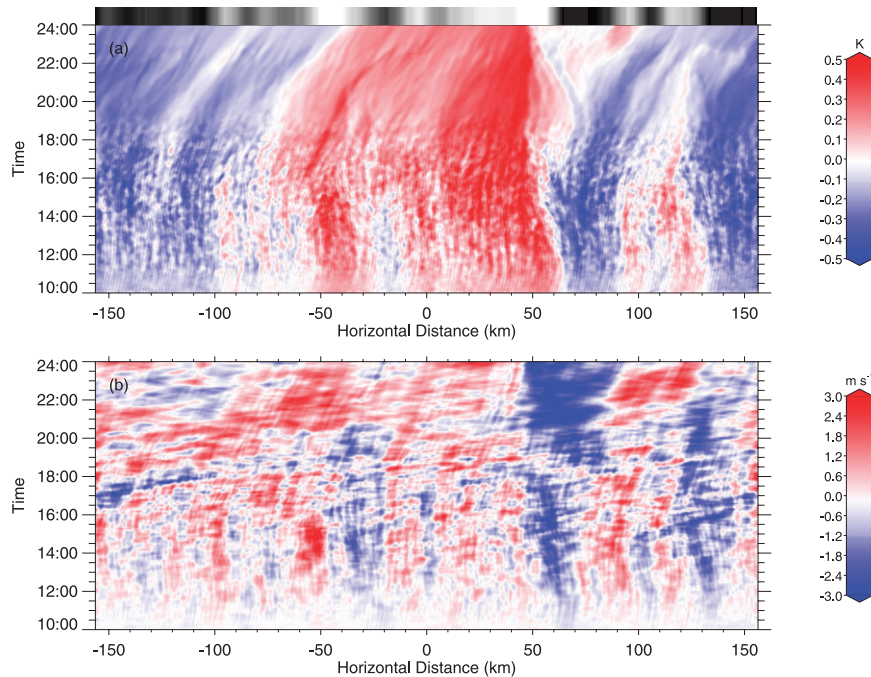
FIG. 3. Hovmöller plots of the difference between HET and CTL at 180-m altitude in (a) θ_e perturbation from the horizontal mean, smoothed with a 2-km-width running mean, and (b) horizontal wind velocity smoothed with a 5-km-width running mean. The grayscale bar shows the Bowen ratio multiplier (white for crop, black for forest).

also compares well with 3D simulations (Avissar and Liu 1996). We would therefore expect the PBL dynamics and initiation of convection, which are the focus of this study, to be well represented in 2D.

To better assess the impact of running in 2D as opposed to 3D, a single additional run was performed (HET3D). This run was the same as HET but with the addition of an extra dimension with a length of 12.5 km. The surface heterogeneity did not vary along this extra dimension, so that the only difference with HET is that the dynamics could develop in 3D. The winds along this extra dimension (i.e., across the domain in HET) were reduced from those in the ECMWF analysis as these were particularly strong and strong winds along vegetation boundaries are known to perturb mesoscale flows (Raasch and Harbusch 2001). A comparison of the cloud cover in HET3D and HET in section 3 confirms the suitability of running the model in 2D.

3. Impact of the surface flux heterogeneity throughout the domain

The heterogeneity in the surface fluxes has a marked impact on the PBL temperatures and winds on the mesoscale throughout the domain. Figure 3 shows the Hovmöller (time–distance) plot of the difference between HET and CTL at 180 m in the potential temperature

perturbation from the horizontal mean, thus removing the impact of the diurnal cycle (Fig. 3a) and the horizontal wind velocity (Fig. 3b). The altitude was chosen as it lies well within the mixed layer and furthermore coincides approximately with the height of the aircraft measurements used in Garcia-Carreras et al. (2010). The mesoscale variability observed in Fig. 3 is due in its entirety to variations present in HET. The anomaly is shown, however, to quantify the magnitude of the variability compared to when surface fluxes are constant.

The imposed surface fluxes have a clear impact on the mixed layer temperatures, with variations of approximately 1 K across vegetation boundaries in HET and very little variability above the kilometer scale in CTL. The magnitude of the temperature variations is comparable to the observations, where temperature anomalies of up to 2 K were observed, with anomalies of 1 K still influencing the winds. This suggests that the magnitude of the imposed flux variability is consistent with observations and in any case not set artificially high. The temperature gradients persist well into the night, with little variation in their magnitude, and remain fairly constant with height.

The heterogeneity in the surface fluxes has an impact on the horizontal wind velocities on the mesoscale (Fig. 3b). There is a mesoscale forcing of the wind analogous
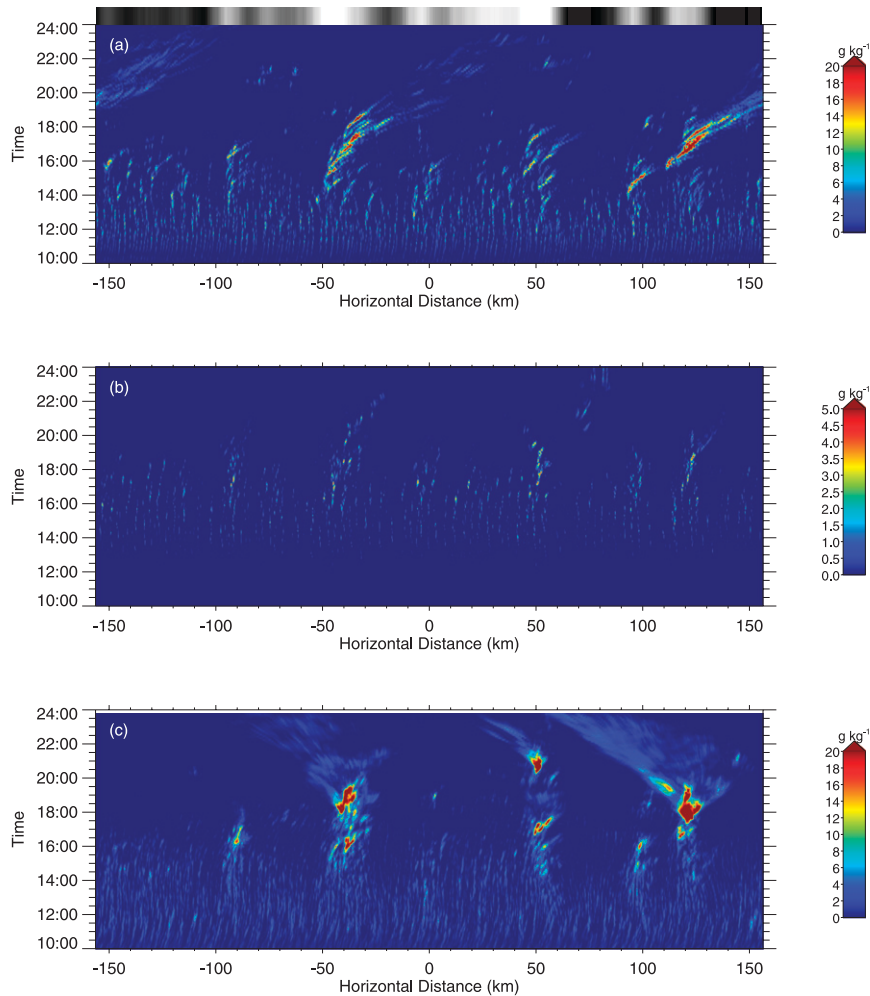
FIG. 4. Hovmöller plots of LWP in (a) HET, (b) HICIN, and (c) HET3D. The grayscale bar shows the Bowen ratio multiplier (white for crop, black for forest).

to that found in the aircraft observations, with low-level divergence over the forest (e.g., at −20 and 70 km) and convergence over the crop (−45, 50, and 120 km). These winds are analogous to gravity currents, with the cooler PBL air over the forest flowing toward the warmer cropland regions. The way the convergence zones move farther into the crop during the afternoon (e.g., from 55 to 45 km between 1200 and 1600 UTC) is consistent with this view. Although not as strong as in the low-level results, there is evidence of a return flow in the cloud level as well, with the wind pattern inverted at 1500 m (not shown). The magnitude of the land-induced wind anomalies (2–4 m s^{-1}) is also comparable to that measured in Garcia-Carreras et al. (2010).

Finally, the presence of these winds organizes cloud cover throughout the domain from early afternoon (Fig. 4a). Clouds are suppressed over the cool anomalies. This is apparent, for example, from −30 to −10, 60 to 90, and

130 to 150 km, where the only substantial clouds present in the afternoon and evening are not locally initiated but rather advected in from the cropland regions. Although clouds form over most of the warmer regions, the clouds over the boundaries between land surface types are consistently deeper. This suggests that the boundaries, where the wind convergence occurs, are the preferred regions for cloud development, although the synoptic conditions are favorable for shallow cloud initiation everywhere in the domain (as demonstrated by the widespread presence of shallow cloud in CTL, not shown). The maximum cloud-top height in HET is also considerably higher than in CTL (6840 m as opposed to 4680 m), suggesting that the heterogeneity adds an extra impetus to the convection in some regions, as well as considerably inhibiting convection in other areas.

Dynamically, the HICIN run is very similar to HET, with perturbations in potential temperature and wind
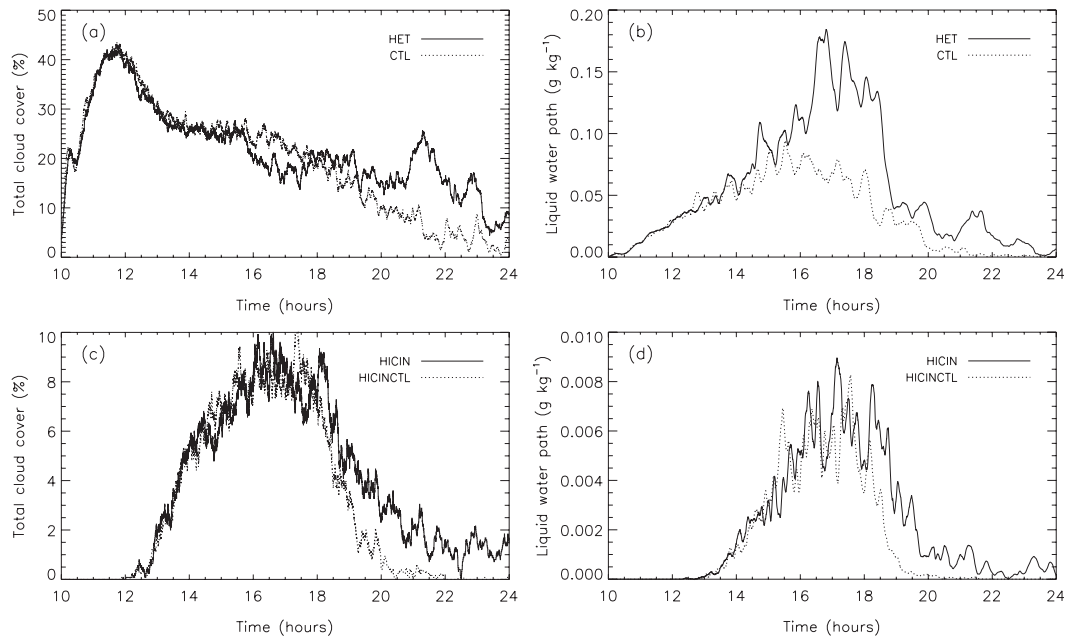
FIG. 5. Domain-averaged (a),(c) cloud cover and (b),(d) LWP for (a),(b) HET and CTL (solid and dotted lines, respectively) and (c),(d) HICIN and HICINCTL (solid and dotted lines, respectively) between 1000 and 0000 UTC.

velocities (not shown) comparable to those shown in Fig. 3. The cloud cover, however, is different because of the inhibition to convection present. Figure 4b shows the liquid water path (LWP) for HICIN (note that the contour scale is considerably smaller than that of Fig. 4a). Cloud-top heights and total liquid water are considerably lower; however, the cloud distribution remains very similar to HET, although the role of the mesoscale convergence zones in deepening clouds only appears later in the afternoon, from about 1600 UTC. The mean convective inhibition is at its lowest and the convective available potential energy at a maximum at this time. This is also when the mesoscale flow is expected to be strongest [as observed, for example, for U.K. sea breezes by Reible et al. (1993)].

The potential temperature and wind perturbations caused by the surface were similar between HET and HET3D (not shown). Figure 4c shows the liquid water path in HET3D averaged across a 2.5-km strip along the middle of the domain. This plot confirms the hypothesis in section 2. The cloud patterns remain largely unvaried between HET and HET3D, with regions of enhanced cloud cover at vegetation boundaries and suppression over the forest. The subsequent evolution of the convection does vary between the two, with stronger convection in HET3D, reaching cloud-top heights close to the domain top, although the location of the deepest clouds is also similar in both runs. A large part of this difference in convective development can be attributed to the reduced winds across the domain, as a 2D run that

used the same wind structure as the 3D run also showed similarly deep convection (not shown). The entrainment in the model is shear dependent, so the reduced shear in HET3D leads to deeper convection, although there might be some impact from the extra dimension as well. The reason that these reduced winds had to be used in the 3D simulation is that whereas in 2D the only impact of the winds across the domain is on entrainment, in 3D the effect of advection is also significant, with winds along land surface boundaries (as would be the case here) affecting the mesoscale flows themselves (Raasch and Harbusch 2001). Regardless of the representation of the full convective development, these results show that the processes responsible for both the initiation of convection and the location of the deepest systems are the same for the two runs and so a 2D modeling setup is appropriate for the questions we seek to answer in this study.

Although the distribution of clouds is clearly influenced by the surface heterogeneity from early in the afternoon, domainwide average properties are relatively similar until a few hours later. Figure 5 shows the differences in cloud cover and liquid water path between HET and CTL as well as between HICIN and HICINCTL. The difference in cloud cover between HET and CTL is insignificant until approximately 1600 UTC, where slightly higher cloud cover is observed in CTL. From 1900 UTC the trend reverses, and the differences between HET and CTL start to increase, with more cloud cover in HET compared to CTL. This is consistent with the organization of cloud in HET. The suppression of
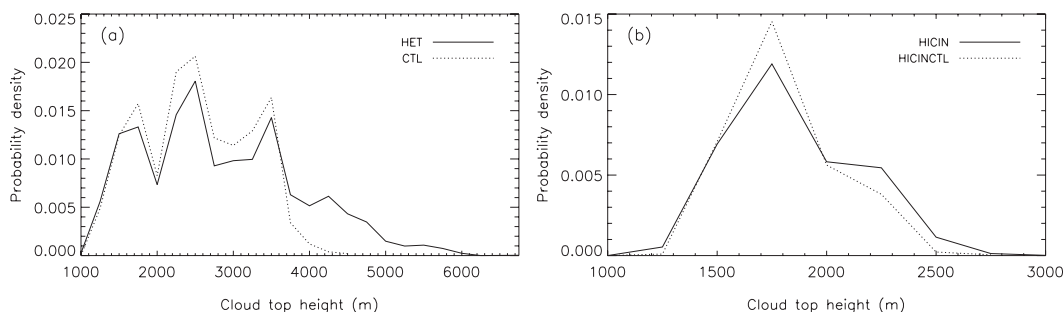
FIG. 6. Histogram of cloud-top heights for (a) HET (solid) and CTL (dotted) and (b) HICIN (solid) and HICINCTL (dotted) using data between 1400 and 1900 UTC.

cloud over the forest slightly reduces the cloud cover in HET during the day. The presence of persistent systems, despite the absence of cold pools, then increases the cloud cover in HET later in the evening. In terms of liquid water path the differences are much larger, occurring between 1530 and 1900 UTC, indicating that even when the cloud cover is lower in HET, the extent of the cloud development is higher. The HICIN runs show a similar pattern, although the differences in liquid water are not as significant.

Looking at the actual distribution of cloud-top heights gives a clearer picture of the potential impact of the differences observed in Fig. 5. Figure 6 shows the probability density function (PDF) of cloud-top heights for all four runs between 1400 and 1900 UTC. Both synoptic conditions (HET/CTL and HICIN/HICINCTL) lead to similar characteristics. The cloud distributions with homogeneous and heterogeneous surface fluxes are similar, with the modal cloud-top height remaining the same (2500 and 1750 m for HET/CTL and HICIN/HICINCTL, respectively). The three peaks in HET are perhaps due to the presence of three stable layers in the vertical profile, although these are not clearly identifiable in Fig. 2. The main difference occurs between the highest cloud-top heights; in HET there are a significant number of clouds above 4000 m, whereas the number in CTL is negligible. In HICIN, the difference is smaller, but still apparent. This difference in higher cloud-top heights becomes more significant in HICIN if later time periods are selected (e.g., 1800–2000 UTC). The presence of a few deeper clouds could have a significant impact on rainfall, particularly if the difference is enough to push certain events toward glaciation and deep convection (not represented here).

4. Mechanisms that cause the organization in cloud cover

a. Thermodynamic effects

To understand the mechanisms that lead from land surface–induced flows to the observed cloud cover

organization in Fig. 4 there are two aspects that need to be explained: (i) why is the boundary between land surface types the region most favorable for the initiation and development of convection, and (ii) why are clouds so strongly suppressed over the forest where the equivalent potential temperature is generally higher [as observed in Betts and Ball (1995) and Alonge et al. (2007) over soil-moisture patches]? To answer these questions, we will be looking more closely at the land surface boundary found at 60 km, since it is the location of the largest gradient in surface fluxes.

A change in the thermodynamic properties of the PBL affects both CAPE and CIN. An increase in equivalent potential temperature θ_e in the boundary layer will increase the CAPE for that air and decrease its CIN. Analysis of the model fields showed that variations in the source air from the boundary layer, rather than variations in the profile, completely dominated variations in CAPE. Therefore, we use the θ_e in the boundary layer as a measure of CAPE. For an adiabatic ascent of a boundary layer parcel above the lifting condensation level (LCL), neglecting condensate loading, if the θ_e of the ascending parcel is greater than the saturated θ_e (θ_{es}, a function of temperature and pressure only) of the profile, it will be buoyant. Therefore, as a measure of CIN, we compare θ_e from the BL with θ_{es} from above the LCL.

Using a similar method to that used in Morcrette et al. (2007), Fig. 7 shows 2-hourly plots of θ_e below the LCL (dotted black line, defined for a parcel originating at 50 m above the ground) and θ_{es} above the LCL for HET, with wind speeds (arrows) and cloud contours (white lines) overplotted. The θ_e flux into the PBL can be shown to be at least approximately constant when the total surface fluxes are constant, as is the case in this simulation (Betts and Ball 1995; also separately verified for this simulation, with a variation less than 2% in θ_e variability observed). Despite this, at 1200 UTC a slight increase in θ_e over the forest compared to the crop is observed. Given the constant flux of θ_e into the PBL at the surface, the higher θ_e over the forest must be due to
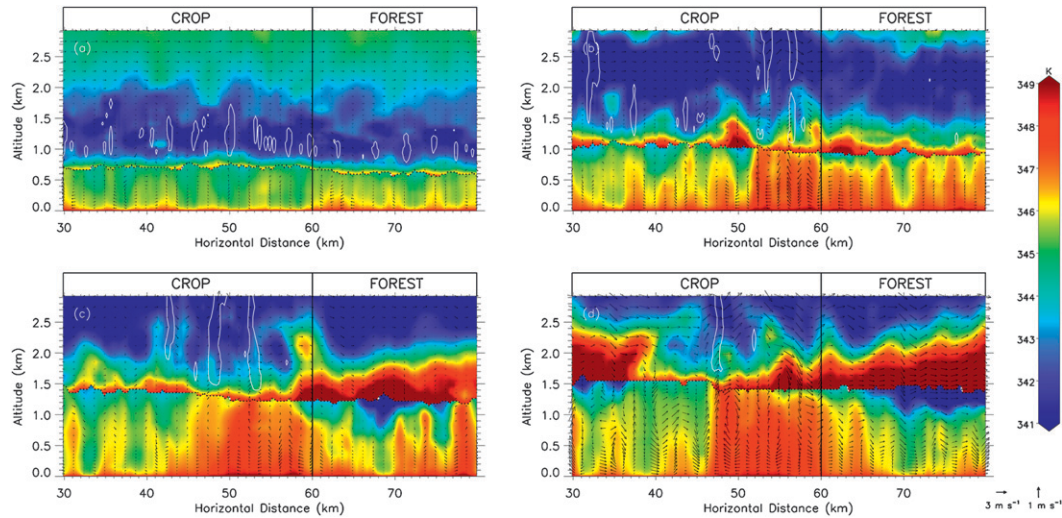
FIG. 7. Two-hourly plots of θ_e (below the LCL, dotted black line) and θ_{es} (above the LCL), for HET at (a) 1200, (b) 1400, (c) 1600, and (d) 1800 UTC. A 2-km running mean smoothing has been applied. Arrows denote wind velocities; white contour lines show the presence of clouds. The vertical black line shows the position of the land surface boundary, with crop to the left and forest to the right.

reduced entrainment of low-θ_e air into the PBL top over the forest as opposed to the crop. This is consistent with the lower PBL height over the forest and the surface θ_e flux entering a smaller volume, thus leading to higher θ_e over the forested regions. This has also been observed for land surfaces with varying soil moisture, where a higher peak in θ_e over wet soils is observed due to lower PBL heights (Betts and Ball 1995; Alonge et al. 2007).

As the day progresses the θ_e peak is advected by the land surface–induced flow from the forest to the crop, leading to a low-level θ_e peak between 50 and 60 km from 1400 UTC (Fig. 7). This coincides with the region of deepest cloud, as observed in Fig. 4a. The peak in θ_e continues to move over the crop between 1400 and 1800 UTC. The presence of a maximum in low-level θ_e at the convergence zones

for the whole domain causes the land surface boundaries, and more specifically the region at the head of the gravity currents, to favor convection. The role of physical convergence, which occurs in the same region and may also be significant, will be explored in the next section.

The reason for the peak in θ_e at the convergence zone, as opposed to either the crop or forest, is related to a reduction in the θ_e fluxes in the PBL. Figure 8 shows the variation in time of the vertical θ_e flux perturbation from the horizontal mean at 700 m (colors), and the θ_e perturbation from the horizontal mean at 200 m (line contours). The different altitudes represent where the variability is of most importance. The θ_e variability originates at the surface and so is most significant at low levels, whereas the θ_e fluxes depend significantly on
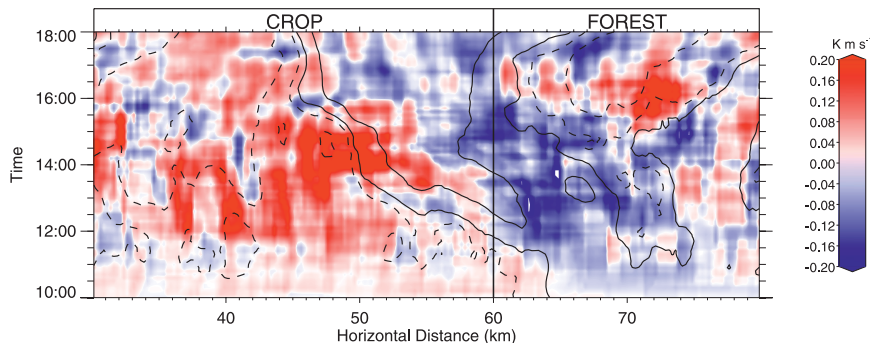

FIG. 8. Hovmöller plot of the vertical θ_e flux perturbation from the horizontal mean at 700 m (colors), and the θ_e perturbation from the horizontal mean at 200 m [contours at $+(-)0.1$ and $+(-)0.5$ K, solid (dashed) lines]. The vertical black line shows the position of the land surface boundary, with crop to the left and forest to the right.
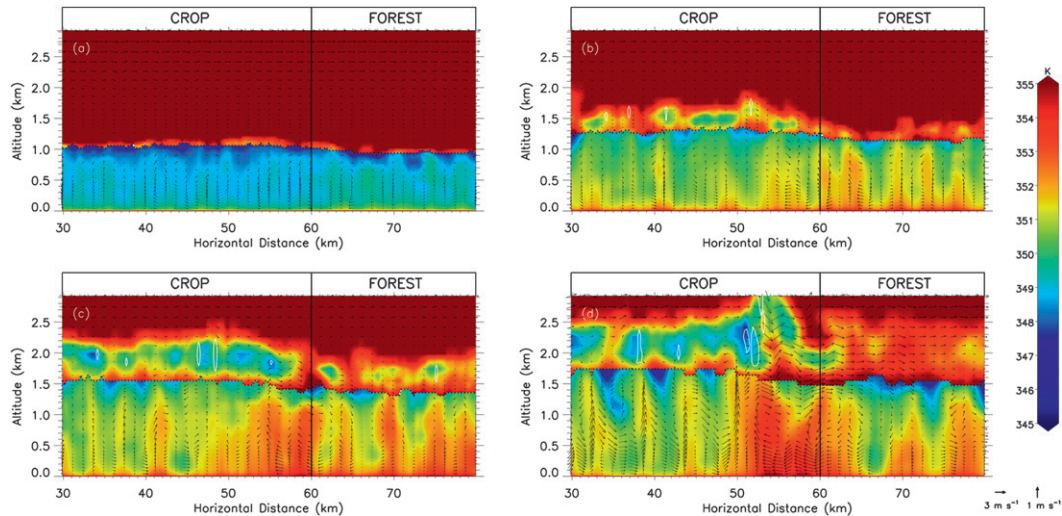
FIG. 9. As in Fig. 7, but for HICIN.

entrainment at the top of the boundary layer. The positive anomaly in θ_e is collocated with a negative anomaly in the θ_e flux, both moving toward the crop during the afternoon. The reduced flux over the forest is consistent with reduced entrainment of low-θ_e air at the PBL top. As the mesoscale flow develops, high-θ_e air is transported toward the crop, where convergence leads to the high-θ_e air being more evenly vertically distributed. This reduction in the vertical θ_e gradient in turn reduces the θ_e flux, thus maintaining high θ_e at the boundary at low levels, while it decreases elsewhere.

At the same time (1400–1800 UTC), a region of high-θ_{es} air develops above the forest PBL, thus forming a strong capping layer that inhibits convection by stabilizing the PBL below (Fig. 7). This leads to negligible cloud cover over the forest throughout the afternoon despite the synoptic conditions favorable to the initiation of shallow clouds. The presence of high-θ_{es} air over the forest could be due to advection of warm crop air at the top of the PBL brought in by the return flow of the mesoscale circulation or to larger-scale subsidence forced by the active convection at the land surface boundary. Differentiating between the two is important in order to estimate the spatial extent and speed over which this suppression occurs.

To further clarify the source of the suppressing layer over the forest, passive tracers emitted at 1200 UTC at the surface between 50 and 60 km (i.e., over the crop boundary) were used to explore the trajectories of this PBL air throughout the afternoon (not shown). The tracers show that although there is a relatively sharp discontinuity in the θ_{es} values above the forest, this cannot be attributed purely to the source of the air (i.e., warm air originating from the crop, with cooler air aloft originating from the

forest), as the tracer crosses this boundary. This suggests that large-scale subsidence is the source of the warming as opposed to the origin of the air mass itself.

The magnitude of the expected warming over the forest due to subsidence can be estimated by using the potential temperature profile to estimate the temperature of the air parcel before it subsides. Taking the lower bound of the mean time-averaged vertical velocity (see section 4b) over the PBL gives a subsidence rate of 0.1 m s^{-1}. This value is consistent with the observed rate of descent of the tracer. The potential temperature gradient above the PBL at 70 km at 1500 UTC, which does not vary appreciably with time, was 4.82×10^{-3} K m^{-1}. The observed descent would then produce a heating at the top of the PBL of approximately 2 K for an hour descent. Comparing the θ_{es} values above the crop and forest in Fig. 7, the difference between the two is of a few degrees (2–3 K), consistent with our estimate.

Figure 9 shows the same results as Fig. 7 but for HICIN. In this case the profile is much more stable, thus inhibiting the convection in the domain. Similar features appear as for HET, although delayed, with an increase in θ_e over the forest, which is then advected over the crop leading to a peak in θ_e over the crop, but close to the boundary. In this case, however, the initiation of convection is not collocated with the peak in θ_e since conditions are too stable. The clouds that do form, however, do so at the leading edge of the mesoscale flow, where updrafts caused by physical convergence are at a maximum. The timing of convection is also delayed compared to HET, as it is only from about 1600 UTC that the boundary layer growth has reduced the convective inhibition sufficiently for triggering to occur. This suggests that in this case moisture convergence has a lesser impact on why clouds form preferentially over the
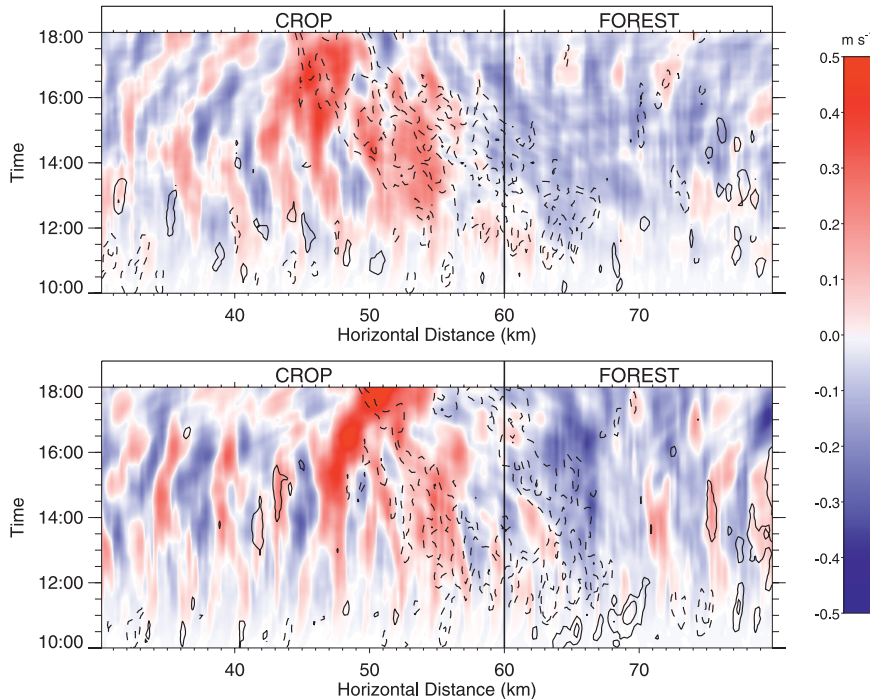
FIG. 10. Hovmöller plots of hourly time averages of vertical wind velocity in (top) HET and (bottom) HICIN at 700 m between 30 and 80 km, with a 5-km running mean applied (colors) and hourly time averages of θ_e gradient at 700 m [line contours at $+(-)0.03$ and $+(-)0.05$ K km^{-1}, solid (dashed) lines]. The vertical black line denotes the land surface boundary, with cropland to the left and forest to the right.

land surface boundaries, whereas physical convergence, which is explored in the following section, could be the dominant mechanism.

b. Dynamical effects

To determine whether physical convergence is a major contributor to the organization of the initiation of convection, the significance of the mesoscale vertical velocity over the total must be ascertained. Figure 10 shows Hovmöller plots of hourly time averages of vertical wind velocity at 700 m, with a 5-km running mean applied for HET and HICIN. The averaging removes the impact of turbulent eddies, thus isolating mesoscale impacts on the updrafts.

In Fig. 10 a persistent updraft can be observed in HET between 50 and 55 km early in the afternoon (1300–1400 UTC), moving farther into the crop to 40–50 km later. HICIN shows a similar pattern. This coincides with the emergence of deeper systems at the crop boundaries as opposed to adjacent crop, as observed in Fig. 4. In both cases the peak in the mesoscale vertical velocity reaches a maximum of approximately 0.5 m s^{-1}. The temperature gradients move with time, and with them the region of peak updrafts. Taking into consideration the averaging

(in space and time), as well as the fact that the peak in the updrafts moves with time, the velocities shown are not only persistent but are also likely to represent a lower bound of the mesoscale impact on the vertical velocities. Although the magnitude of the mesoscale vertical velocity is high, it is nonlinear (narrow updrafts surrounded by gentler, broader subsidence), and the domain-mean impact is small.

As well as highlighting the regions of mesoscale convergence, Fig. 10 shows a region of subsidence over the forest. The fact that the subsidence covers a relatively large area in both runs is consistent with large-scale subsidence, as concluded in section 4a. The magnitude of the descent is on the order of 0.1–0.2 m s^{-1}.

In both HET and HICIN the movement of the peak updraft into the crop follows the temperature gradients (dashed contour lines). Their relative position, however, highlights a difference between the two cases. Whereas in HET the updrafts are located within the minimum in temperature gradient (e.g., at 53 km, 1400 UTC), in HICIN the updrafts occur ahead of the temperature gradient (when oriented along the mesoscale flow direction). This is consistent with Figs. 7 and 9, which suggest that in HET convection is initiated within the
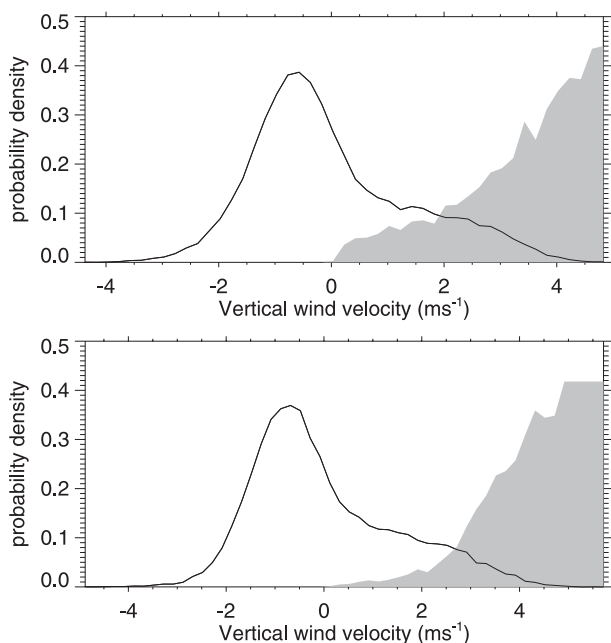
FIG. 11. PDF of vertical velocity at an altitude of 700 m for (top) CTL and (bottom) HICINCTL for all the data (line) and the proportion of points where moist convection had been recently initiated (shading; see text for details). Data taken between 1400 and 1700 UTC.

mesoscale flow, where θ_e is maximum, whereas in HICIN the initiation of convection occurs at the leading edge of the mesoscale flow. The resulting difference in cloud patterns is small, as in both cases there is enhanced convection in the boundary of the warm anomaly, but it highlights the difference in the cause of the observed pattern.

The lines in Fig. 11 show the PDF of vertical velocities for CTL (Fig. 11, top) and HICINCTL (Fig. 11, bottom) at an altitude of 700 m. Data between 1400 and 1700 UTC are used, as it is during these times that the mesoscale impact is maximized. The shaded contour shows the PDF of the proportion of updrafts at the same altitude which initiate convection. A point was assumed to have initiated convection if it had cloud above and there was a persistent updraft (the vertical velocity had to exceed 0.1 m s^{-1} at that time and 6 min before), in order to remove the impact of clouds advected in as opposed to initiated locally.

The distribution of vertical velocities is similar in the two runs, as the surface forcings are the same in both cases. There is, however, a difference in the distribution of vertical velocities associated with the initiation of convection. In HET (Fig. 11, top) initiation occurs for all vertical velocities, although there is a preference for higher velocities. This is due to the lack of CIN in the profile, suggesting that the updraft strength is not the

limiting factor for the initiation of convection. In Fig. 11, bottom, however, the cloud distribution is heavily skewed toward the high vertical velocities, with little initiation of convection when vertical velocities are below 1 m s^{-1}. In this case convection will only be initiated when sufficient updraft strength exists to overcome the inhibition present.

With a variable land surface, mesoscale convergence consistently contributes approximately 0.5 m s^{-1} over the convergence zones (Fig. 10; the exact distribution of vertical velocities at the convergence zone is unknown because of the lack of statistics over such a narrow area). The maximum vertical velocity over the time period sampled for the PDF (1400–1700 UTC), however, is similar, if not higher, over the convergence zone compared to the crop. This implies that the increase in the mean vertical velocity observed at the convergence zone must produce more updrafts with velocities greater than 1 m s^{-1}, thus causing deeper and more persistent cloud cover associated with it. These results suggest, as hypothesized at the end of section 4a, that although the cloud cover pattern is similar in both HET and HICIN, in HET the major factor in producing this pattern is moisture convergence, whereas in HICIN it is physical convergence and lifting. The timing of convection in both runs is consistent with this conclusion. In HET the heterogeneity in cloud cover becomes apparent from 1400 UTC, when the mesoscale flows begin to dominate. In HICIN, convection is delayed until 1600 UTC, as two conditions must be met: sufficient physical convergence and lifting (associated with the mesoscale flows, from 1400 UTC) and a sufficiently weak inhibiting barrier, which is eroded by the growing boundary layer throughout the afternoon.

A distinction has been made between the impacts of thermodynamic and dynamic effects on the initiation of convection, since these are separate effects in terms of their influences on the potential and kinetic energy of a developing cumulus cell. However, it is worth pointing out that the causes of these thermodynamic and dynamic effects are not purely independent. The thermodynamic effect described is caused by mesoscale convergence (i.e., a dynamic effect) in the first place. Therefore, even if in HET convergence and lifting are not directly responsible for the observed cloud pattern, it is the mechanism that allows θ_e to build up, so that an increase in the mesoscale circulations will increase the magnitude of both effects. On the other hand, the reverse is not true, as an increase in θ_e does not then feed back directly into the mesoscale circulation.

Our final hypothesis as to possible mechanisms for the land–atmosphere coupling was that the higher turbulence over the crop led to a higher frequency of cloud-forming
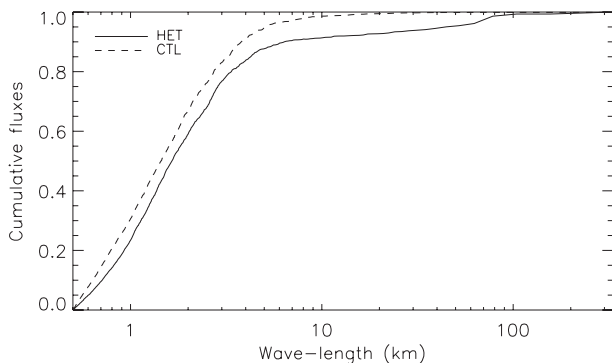
FIG. 12. Domain-mean heat fluxes at 500 m averaged between 1400 and 1700 UTC as a function of length scale for HET (solid) and CTL (dashed).

FIG. 13. Domain-mean heat flux profiles at 1400 (black), 1500 (red), and 1600 (green) UTC for HET (solid) and CTL (dashed).

thermals, as opposed to any impact from the mesoscale flows. We have seen so far that the mesoscale circulations are able to explain the cloud pattern that is observed. Furthermore, neither the liquid water path nor the cloud-top height is merely a function of sensible heat flux, as would occur if turbulence were the dominant mechanism. For example, the sensible heat fluxes are approximately the same at 30 and 115 km, but the cloud cover in the latter is considerably more organized and intense (Fig. 4a). The presence of a positive peak in the horizontally and time-averaged vertical velocities in the regions of cloud formation also suggests that mesoscale convergence, and not enhanced turbulence, is the cause of the observed cloud patterns.

It is of interest to look at the impact of the heterogeneous surface fluxes on mid-PBL fluxes, a somewhat contentious issue in the literature as outlined in section 1. In terms of domain-mean heat and humidity fluxes, the differences between HET and CTL are overall negligible when aggregated throughout the afternoon. This, however, does not diminish the importance of correctly characterizing the land surface. Figure 12 shows a cumulative plot of the heat fluxes at 500 m as a function of length scale averaged throughout the domain and between 1400 and 1700 UTC. The fluxes for each length scale were normalized by the total flux in the run. Figure 12 shows that although the total fluxes in HET and CTL are approximately the same, the large majority of this arises from small scales in CTL, whereas there is a 10%–15% contribution from mesoscale fluxes in HET, depending on the cutoff wavelength chosen (4–6 km). This mesoscale component lies primarily at wavelengths of 60–70 km, consistent with the size of the heterogeneities.

Figure 13 shows the vertical profiles of the PBL heat fluxes at three different times, which highlights another difference between HET and CTL. Although PBL fluxes are the same between the two runs, the fluxes just above
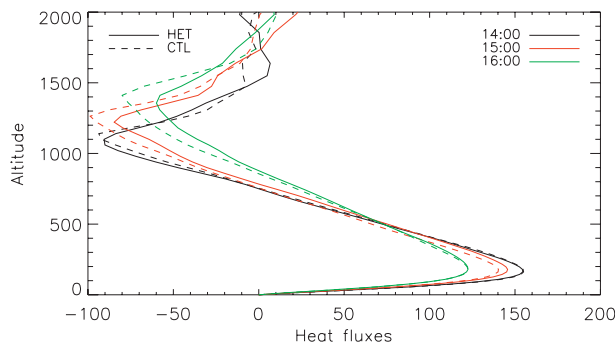
the PBL differ significantly, with lower downward fluxes in HET indicating a reduction in the entrainment rates. This is consistent with the results shown so far as entrainment is lower over the mesoscale updrafts, and elsewhere the profile is stabilized above the PBL top due to subsidence, again limiting the entrainment. This seems to lead to a marginally lower mean PBL height in CTL from 1500 UTC. These results are similar to what was found by Huang and Margulis (2009) for roll convection.

5. Conclusions and discussion

The focus of this study was to determine the exact mechanism that leads to the initiation of convective cloud within mesoscale convergence zones over heterogeneous vegetation. The aircraft track from Garcia-Carreras et al. (2010) was used as a case study for a 2D simulation using the Met Office Large Eddy Model. Surface fluxes were imposed using ground station data from Nangatchori, Benin, and the heterogeneity was derived using the land-cover data used in Garcia-Carreras et al. (2010), increasing the Bowen ratio over crop, and decreasing it over forest, keeping total surface and therefore θ_e fluxes constant. Runs with a homogeneous (CTL) land surface and heterogeneous (HET) surface were completed. Another run wherein CIN was increased was also performed (HICIN), to compare with the low-CIN conditions found in HET.

The heterogeneous land surface created temperature differences between cropland and forested areas consistent with observations (approximately 1 K at land surface boundaries). These gradients then forced mesoscale winds, organizing cloud cover with enhanced convection over the crop boundaries and suppression of convection over the forest, again consistent with aircraft observations. Although the cloud cover in HET was more extensive than in HICIN, due to synoptic conditions more favorable to convective development, the overall cloud pattern was found to be very similar.

Analysis of the model data shows that the optimum conditions for the initiation of convection are found on the warm side of the boundary. Because of lower sensible heat fluxes and thus reduced entrainment at the PBL top, the PBL θ_e is initially higher over the forest as opposed to the crop, although the flux of θ_e from the surface into the PBL was constant everywhere. The mesoscale flow, however, advects and vertically mixes high-θ_e air over the crop boundary. The resultant reduced vertical θ_e flux at the boundary maintains high θ_e values at the convergence zone compared to the adjacent crop and forest, thus leading to a domain maximum θ_e at the convergence zones, which promotes convective development in this region. Furthermore, physical convergence forces persistent vertical velocities of up to 0.5 m s^{-1} at the boundary. Both these mechanisms combine to enhance the initiation of convection at the crop boundaries. A peak in θ_e or CAPE has been observed at mesoscale convergence lines before (Trier et al. 2004; Wakimoto and Murphey 2010). However, for the first time we outline in detail how the mesoscale convergence itself can produce the peak in θ_e. These results are also consistent with Zhang and Klein (2010), who attribute the transition from shallow to deep convection to parcels with the highest moisture values in the PBL and with enhanced vertical momentum caused by, for example, mesoscale wind variability in the PBL.

The relative importance of these two mechanisms depends on the synoptic conditions. In HET, the lack of CIN means that there is a very small barrier for convection to be initiated, and therefore the peak in θ_e in the PBL at the crop boundaries dominates the observed cloud cover patterns. In HICIN, on the other hand, conditions are particularly stable and thus there is a minimum vertical velocity of approximately 1 m s^{-1} needed to overcome CIN. In this case, the increase in the updraft strength caused by the mesoscale convergence is likely to be the dominant cause of the observed cloud pattern.

The mesoscale flows also lead to descent above the mixed layer over the forest at an approximate rate of 0.1 m s^{-1}. The cause of the subsidence could be a consequence of the developing convection at the crop boundaries, descent associated with divergence over the forest due to the mesoscale flow, or a combination of the two. The heating associated with the observed descent can be estimated to be of 2 K in these cases. This layer of warm air over the forest stabilizes the PBL, suppressing the initiation of convection over the forest throughout the afternoon and further reducing entrainment (Parker 2002).

Future work will consider the impact on these results of using a fully coupled land surface model to explore the effect of potential feedback mechanisms (such as the effect of cloud shading, which will predominate in the

warmer regions) on the PBL dynamics. Extending the modeling approach to a full 3D simulation would also allow a better quantification of the impact of the surface on cloud properties.

Domain-mean thermodynamic and dynamical properties do not vary considerably with mesoscale surface heterogeneities, but the distribution of clouds, cloud-top heights, and the persistence of such systems do. Further work is needed to evaluate the impact of such changes at larger scales, particularly the impact for GCM-type simulations where mesoscale processes are unresolved. Other mechanisms by which the mesoscale could affect larger-scale dynamics also need to be better understood. Some examples include their influence on large-scale flows, such as the monsoon, the impact of the moistening of the middle troposphere by persistent clouds, the direct initiation of deep convective systems, which can influence the atmosphere and land surface over a large area downwind, and the impact of mesoscale flows on propagating mesoscale convective systems. Observations of the initiation of a mesoscale convective system via the interaction between a gravity wave propagating from a remote mature storm and soil-moisture patches provide one example of the potential interactions between mesoscale and synoptic processes (Taylor et al. 2010). An evaluation of the impact of the land surface on rainfall will also be of particular interest, as this provides the main feedback from the atmosphere to the land surface, both at the diurnal and seasonal time scales (Taylor et al. 2003).

REFERENCES

Alonge, C. J., K. I. Mohr, and W. K. Tao, 2007: Numerical studies of wet versus dry soil regimes in the West African Sahel. *J. Hydrometeor.,* **8,** 102–116.

Avissar, R., and Y. Liu, 1996: Three-dimensional numerical study of shallow convective clouds and precipitation induced by land surface forcing. *J. Geophys. Res.,* **101,** 7499–7518.

——, and T. Schmidt, 1998: An evaluation of the scale at which ground-surface heat flux patchiness affects the convective

boundary layer using large-eddy simulations. *J. Atmos. Sci.,* **55,** 2666–2689.

Betts, A. K., and J. H. Ball, 1995: The FIFE surface diurnal cycle climate. *J. Geophys. Res.,* **100,** 25 679–25 693.

——, R. L. Desjardins, and D. Worth, 2007: Impact of agriculture, forest and cloud feedback on the surface energy budget in BOREAS. *Agric. For. Meteor.,* **142,** 156–169.

Brown, M. E., and D. L. Arnold, 1998: Land–surface–atmosphere interactions associated with deep convection in Illinois. *Int. J. Climatol.,* **18,** 1637–1653.

Chen, F., and R. Avissar, 1994: The impact of land-surface wetness heterogeneity on mesoscale heat fluxes. *J. Appl. Meteor.,* **33,** 1323–1340.

Chen, T.-C., J.-H. Yoon, K. J. St. Croix, and E. S. Takle, 2001: Suppressing impacts of the Amazonian deforestation by the global circulation change. *Bull. Amer. Meteor. Soc.,* **82,** 2209–2216.

Chu, P. S., Z. P. Yu, and S. Hastenrath, 1994: Detecting climate change concurrent with deforestation in the Amazon basin: Which way has it gone? *Bull. Amer. Meteor. Soc.,* **75,** 579–583.

Cutrim, E., D. W. Martin, and R. Rabin, 1995: Enhancement of cumulus clouds over deforested lands in Amazonia. *Bull. Amer. Meteor. Soc.,* **76,** 1801–1805.

Doran, J. C., and S. Zhong, 2000: A study of the effects of sub-grid-scale land use differences on atmospheric stability in prestorm environments. *J. Geophys. Res.,* **105,** 9381–9392.

——, W. J. Shaw, and J. M. Hubbe, 1995: Boundary layer characteristics over areas of inhomogeneous surface fluxes. *J. Appl. Meteor.,* **34,** 559–571.

Fabry, F., 2006: The spatial variability of moisture in the boundary layer and its effect on convection initiation: Project-long characterization. *Mon. Wea. Rev.,* **134,** 79–91.

Frye, J. D., and T. L. Mote, 2010: Convection initiation along soil moisture boundaries in the southern Great Plains. *Mon. Wea. Rev.,* **138,** 1140–1151.

Garcia-Carreras, L., D. J. Parker, C. M. Taylor, C. E. Reeves, and J. G. Murphy, 2010: Impact of mesoscale vegetation heterogeneities on the dynamical and thermodynamic properties of the planetary boundary layer. *J. Geophys. Res.,* **115,** D03102, doi:10.1029/2009JD012811.

Gray, M. E. B., J. Petch, S. H. Derbyshire, A. R. Brown, A. P. Lock, H. A. Swann, and P. R. A. Brown, 2001: Version 2.3 of the Met Office large eddy model. Part II: Scientific documentation. Met Office, 49 pp. [Available online at http://appconv.metoffice.com/LEM/docs.html.]

Huang, H.-Y., and S. A. Margulis, 2009: On the impact of surface heterogeneity on a realistic convective boundary layer. *Water Resour. Res.,* **45,** W04425, doi:10.1029/2008WR007175.

Kang, S.-L., and K. J. Davis, 2008: The effects of mesoscale surface heterogeneity on the fair-weather convective atmospheric boundary layer. *J. Atmos. Sci.,* **65,** 3197–3213.

——, and ——, 2009: Reply. *J. Atmos. Sci.,* **66,** 3229–3232.

——, ——, and M. LeMone, 2007: Observations of the ABL structures over a heterogeneous land surface during IHOP_2002. *J. Hydrometeor.,* **8,** 221–244.

Kawase, H., T. Yoshikane, M. Hara, F. Kimura, T. Sato, and S. Ohsawa, 2008: Impact of extensive irrigation on the formation of cumulus clouds. *Geophys. Res. Lett.,* **35,** L01806, doi:10.1029/2007GL032435.

Khairoutdinov, M. F., and D. A. Randall, 2003: Cloud resolving modeling of the ARM summer 1997 IOP: Model formulation, results, uncertainties, and sensitivities. *J. Atmos. Sci.,* **60,** 607–625.

Kim, H. J., Y. Noh, and S. Raasch, 2004: Interaction between wind and temperature fields in the planetary boundary layer for a spatially heterogeneous surface heat flux. *Bound.-Layer Meteor.,* **111,** 225–246.

Mahrt, L., J. L. Sun, D. Vickers, J. I. Macpherson, J. R. Pederson, and R. L. Desjardins, 1994: Observations of fluxes and inland breezes over a heterogeneous surface. *J. Atmos. Sci.,* **51,** 2484–2499.

Marsham, J. H., C. J. Morcrette, K. A. Browning, A. M. Blyth, D. J. Parker, U. Corsmeier, N. Kalthoff, and M. Kohler, 2007a: Variable cirrus shading during initiation of CSIP IOP 5. I: Effects on the initiation of convection. *Quart. J. Roy. Meteor. Soc.,* **133,** 1643–1660.

——, and Coauthors, 2007b: Variable cirrus shading during CSIP IOP 5. II: Effects on the convective boundary layer. *Quart. J. Roy. Meteor. Soc.,* **133,** 1661–1675.

——, D. J. Parker, C. M. Grams, B. T. Johnson, W. M. F. Grey, and A. N. Ross, 2008: Observations of mesoscale and boundary-layer scale circulations affecting dust transport and uplift over the Sahara. *Atmos. Chem. Phys.,* **8,** 6979–6993.

McGuffie, K., A. Henderson-Sellers, H. Zhang, T. B. Durbridge, and A. J. Pitman, 1995: Global climate sensitivity to tropical deforestation. *Global Planet. Change,* **10,** 97–128.

Morcrette, C., H. Lean, K. Browning, J. Nicol, N. Roberts, P. Clark, A. Russell, and A. Blyth, 2007: Combination of mesoscale and synoptic mechanisms for triggering an isolated thunderstorm: Observational case study of CSIP IOP 1. *Mon. Wea. Rev.,* **135,** 3728–3749.

Negri, A. J., R. F. Adler, L. M. Xu, and J. Surratt, 2004: The impact of Amazonian deforestation on dry season rainfall. *J. Climate,* **17,** 1306–1319.

Ookouchi, Y., M. Segal, R. C. Kessler, and R. A. Pielke, 1984: Evaluation of soil moisture effects on the generation and modification of mesoscale circulations. *Mon. Wea. Rev.,* **112,** 2281–2292.

Parker, D. J., 2002: The response of CAPE and CIN to tropospheric thermal variations. *Quart. J. Roy. Meteor. Soc.,* **128,** 119–130.

Patton, E. G., P. P. Sullivan, and C. H. Moeng, 2005: The influence of idealized heterogeneity on wet and dry planetary boundary layers coupled to the land surface. *J. Atmos. Sci.,* **62,** 2078–2097.

Petch, J. C., P. N. Blossey, and C. S. Bretherton, 2008: Differences in the lower troposphere in two- and three-dimensional cloud-resolving model simulations of deep convection. *Quart. J. Roy. Meteor. Soc.,* **134,** 1941–1946.

Pielke, R. A., 2001: Influence of the spatial distribution of vegetation and soils on the prediction of cumulus convective rainfall. *Rev. Geophys.,* **39,** 151–177.

——, J. Adegoke, A. Beltran-Przekurat, C. A. Hiemstra, J. Lin, U. S. Nair, D. Niyogi, and T. E. Nobis, 2007: An overview of regional land-use and land-cover impacts on rainfall. *Tellus,* **59B,** 587–601.

Prabha, T. V., A. Karipot, and M. W. Binford, 2007: Characteristics of secondary circulations over an inhomogeneous surface simulated with large-eddy simulation. *Bound.-Layer Meteor.,* **123,** 239–261.

Raasch, S., and G. Harbusch, 2001: An analysis of secondary circulations and their effects caused by small-scale surface inhomogeneities using large-eddy simulation. *Bound.-Layer Meteor.,* **101,** 31–59.

Rabin, R. M., S. Stadler, P. J. Wetzel, D. J. Stensrud, and M. Gregory, 1990: Observed effects of landscape variability on convective clouds. *Bull. Amer. Meteor. Soc.,* **71,** 272–280.

Reible, D. D., J. E. Simpson, and P. F. Linden, 1993: The sea breeze and gravity-current frontogenesis. *Quart. J. Roy. Meteor. Soc.,* **119,** 1–16.

Roy, S. B., 2009: Mesoscale vegetation–atmosphere feedbacks in Amazonia. *J. Geophys. Res.,* **114,** D20111, doi:10.1029/2009JD012001.

——, and R. Avissar, 2002: Impact of land use/land cover change on regional hydrometeorology in Amazonia. *J. Geophys. Res.,* **107,** 8037, doi:10.1029/2000JD000266.

Segal, M., and R. W. Arritt, 1992: Nonclassical mesoscale circulations caused by surface sensible heat-flux gradients. *Bull. Amer. Meteor. Soc.,* **73,** 1593–1604.

——, R. Avissar, M. C. McCumber, and R. A. Pielke, 1988: Evaluation of vegetation effects on the generation and modification of mesoscale circulations. *J. Atmos. Sci.,* **45,** 2268–2293.

Smith, E. A., M. M.-K. Wai, H. J. Cooper, and M. T. Rubes, 1994: Linking boundary-layer circulations and surface processes during FIFE 89. Part I: Observational analysis. *J. Atmos. Sci.,* **51,** 1497–1529.

Souza, E. P., N. O. Rennó, and M. A. F. Silva Dias, 2000: Convective circulations induced by surface heterogeneities. *J. Atmos. Sci.,* **57,** 2915–2922.

Taylor, C. M., R. J. Ellis, D. J. Parker, R. R. Burton, and C. D. Thorncroft, 2003: Linking boundary-layer variability with convection: A case-study from JET2000. *Quart. J. Roy. Meteor. Soc.,* **129,** 2233–2253.

——, D. J. Parker, and P. P. Harris, 2007: An observational case study of mesoscale atmospheric circulations induced by soil moisture. *Geophys. Res. Lett.,* **34,** L15801, doi:10.1029/2007GL030572.

——, P. P. Harris, and D. J. Parker, 2010: Impact of soil moisture on the development of a Sahelian mesoscale convective system: A case-study from the AMMA special observing period. *Quart. J. Roy. Meteor. Soc.,* **136,** 456–470.

Trier, S. B., F. Chen, and K. W. Manning, 2004: A study of convection initiation in a mesoscale model using high-resolution land surface initial conditions. *Mon. Wea. Rev.,* **132,** 2954–2976.

Wakimoto, R. M., and H. V. Murphey, 2010: Analysis of convergence boundaries observed during IHOP_2002. *Mon. Wea. Rev.,* **138,** 2737–2760.

Wang, J. F., R. L. Bras, and E. A. B. Eltahir, 2000: The impact of observed deforestation on the mesoscale distribution of rainfall and clouds in Amazonia. *J. Hydrometeor.,* **1,** 267–286.

——, and Coauthors, 2009: Impact of deforestation in the Amazon basin on cloud climatology. *Proc. Natl. Acad. Sci. USA,* **106,** 3670–3674.

Weaver, C. P., 2004a: Coupling between large-scale atmospheric processes and mesoscale land–atmosphere interactions in the U.S. southern Great Plains during summer. Part I: Case studies. *J. Hydrometeor.,* **5,** 1223–1246.

——, 2004b: Coupling between large-scale atmospheric processes and mesoscale land–atmosphere interactions in the U.S. southern Great Plains during summer. Part II: Mean impacts of the mesoscale. *J. Hydrometeor.,* **5,** 1247–1258.

——, 2009: Comments on ''The effects of mesoscale surface heterogeneity on the fair-weather convective atmospheric boundary layer.'' *J. Atmos. Sci.,* **66,** 3226–3228.

——, and R. Avissar, 2001: Atmospheric disturbances caused by human modification of the landscape. *Bull. Amer. Meteor. Soc.,* **82,** 269–281.

Werth, D., and R. Avissar, 2002: The local and global effects of Amazon deforestation. *J. Geophys. Res.,* **107,** 8087, doi:10.1029/2001JD000717.

Wilson, J. W., and W. E. Schreiber, 1986: Initiation of convective storms at radar-observed boundary-layer convergence lines. *Mon. Wea. Rev.,* **114,** 2516–2536.

Xu, K.-M., and Coauthors, 2002: An intercomparison of cloud-resolving models with the atmospheric radiation measurement summer 1997 intensive observation period data. *Quart. J. Roy. Meteor. Soc.,* **128,** 593–624.

Zhang, H., A. Henderson-Sellers, and K. McGuffie, 2001: The compounding effects of tropical deforestation and greenhouse warming on climate. *Climatic Change,* **49,** 309–338.

Zhang, Y., and S. A. Klein, 2010: Mechanisms affecting the transition from shallow to deep convection over land: Inferences from observations of the diurnal cycle collected at the ARM Southern Great Plains site. *J. Atmos. Sci.,* **67,** 2943–2959.

Zhong, S., and J. C. Doran, 1998: An evaluation of the importance of surface flux variability on GCM-scale boundary-layer characteristics using realistic meteorological and surface forcing. *J. Climate,* **11,** 2774–2788.

Ziegler, C. L., and E. N. Rasmussen, 1998: The initiation of moist convection at the dryline: Forecasting issues from a case study perspective. *Wea. Forecasting,* **13,** 1106–1131.